AFRL-AFOSR-CL-TR-2017-0005

Space Object Detection & Tracking Within a Finite Set Statistics Framework

Martin Adams
Department of Electrical Engineering, Universidad de Chile

04/13/2017
Final Report

Air Force Research Laboratory
AF Office Of Scientific Research (AFOSR)/ IOS
Arlington, Virginia 22203
Air Force Materiel Command

REPORT DOCUMENTATION PAGE

Form Approved
OMB No. 0704-0188

1. REPORT DATE *(DD-MM-YYYY)*	2. REPORT TYPE	3. DATES COVERED *(From - To)*
21-04-2017	Final	01 Feb 2015 to 31 Jan 2017

4. TITLE AND SUBTITLE
Space Object Detection & Tracking Within a Finite Set Statistics Framework

5a. CONTRACT NUMBER

5b. GRANT NUMBER
FA9550-15-1-0069

5c. PROGRAM ELEMENT NUMBER
61102F

6. AUTHOR(S)
Martin Adams

5d. PROJECT NUMBER

5e. TASK NUMBER

5f. WORK UNIT NUMBER

7. PERFORMING ORGANIZATION NAME(S) AND ADDRESS(ES)
Department of Electrical Engineering, Universidad de Chile
Av. Tupper 2007
Santiago, 8370451 CL

8. PERFORMING ORGANIZATION REPORT NUMBER

9. SPONSORING/MONITORING AGENCY NAME(S) AND ADDRESS(ES)
AFOSR/SOARD
U.S. Embassy Santiago
Av. Andres Bello 2800
Santiago, Chile

10. SPONSOR/MONITOR'S ACRONYM(S)
AFRL/AFOSR IOS

11. SPONSOR/MONITOR'S REPORT NUMBER(S)
AFRL-AFOSR-CL-TR-2017-0005

12. DISTRIBUTION/AVAILABILITY STATEMENT
A DISTRIBUTION UNLIMITED: PB Public Release

13. SUPPLEMENTARY NOTES

14. ABSTRACT

This report provides a summary of the work carried out in the second year of the SOARD project, Grant No. FA9550-15-1-0069, devoted to the investigation and improvement of the detection and tracking methods of inactive Resident Space Objects (RSOs). In the second year, a Random Finite Set (RFS) based Joint Target Detection and Tracking lter was evaluated for the space object tracking scenarios and two extensions were developed in order to increase their robustness to unknown detection statistics. The performance of the extensions was evaluated using both simulated and real data from the Chilbolton Advanced Meteorological Radar (CAMRa). Both pre-processed and raw data sets from the CAMRa were obtained. In the pre-processed data set, a maximum of one detection was reported per bearing angle based on detection methods used at the CAMRa site. The raw data was also processed by using a Constant False Alarm Rate algorithm that was able to report multiple detections per bearing angle, increasing the probability of detecting the target of interest.

15. SUBJECT TERMS

16. SECURITY CLASSIFICATION OF:			17. LIMITATION OF ABSTRACT	18. NUMBER OF PAGES	19a. NAME OF RESPONSIBLE PERSON
a. REPORT	b. ABSTRACT	c. THIS PAGE			MARTINEZ, MICHAEL
Unclassified	Unclassified	Unclassified	SAR	31	19b. TELEPHONE NUMBER *(Include area code)* 571-289-5167

SOARD Project Report: Space Object Detection and Tracking Within a Finite Set Statistics Framework
Grant No. FA9550-15-1-0069
Period of Performance: 1 February 2016 - 31 January 2017

Prof. Martin Adams*, Andrey Pak, MSc.†, Javier Correa, PhD.‡ and Leonardo Cament, PhD.§

Department of Electrical Engineering , Universidad de Chile

January 28, 2017

*Project PI, martin@ing.uchile.cl
†ap360@hw.ac.uk
‡javier.correa@amtc.cl
§lcament@ing.uchile.cl

Abstract

This report provides a summary of the work carried out in the second year of the SOARD project, Grant No. FA9550-15-1-0069, devoted to the investigation and improvement of the detection and tracking methods of inactive Resident Space Objects (RSOs).

In the second year, a Random Finite Set (RFS) based Joint Target Detection and Tracking filter was evaluated for the space object tracking scenarios and two extensions were developed in order to increase their robustness to unknown detection statistics. The performance of the extensions was evaluated using both simulated and real data from the Chilbolton Advanced Meteorological Radar (CAMRa). Both pre-processed and raw data sets from the CAMRa were obtained. In the pre-processed data set, a maximum of one detection was reported per bearing angle based on detection methods used at the CAMRa site. The raw data was also processed by using a Constant False Alarm Rate algorithm that was able to report multiple detections per bearing angle, increasing the probability of detecting the target of interest. Tracking algorithms, based on the RFS-based Joint Target Detection and Tracking (JoTT) filter were investigated, which also include the estimation of target detection statistics, parameters which are often difficult to determine, and which can be time varying. In all cases, qualitative and quantitative improvements in the robustness of the proposed tracking methods were observed when comparing with the standard JoTT filter.

In addition, image sequences from the Georgia Tech observatory, known as the Omnidirectional Space Situational Awareness (OmniSSA) data set, were processed to determine the feasibility of applying the RFS filtering concepts to image data.

Contents

List of Figures

1 Introduction

The growing number of inactive RSOs poses a real threat to future space missions and has provoked an increased need for developing robust methods of orbital object tracking. As an example, the Chinese anti-satellite weapon test in 2007 and the unintentional collision of the Cosmos-2251 and Iridium-33 satellites in 2009 are estimated to have produced almost 36% of the total number of currently tracked objects in the Low-Earth Orbit (LEO) [18]. Currently, the number of objects being tracked by the U.S. Space Surveillance Network (SSN) exceeds 21,000 targets and mainly consists of objects which have an effective diameter larger than 10cm [18].

Detecting and tracking these objects is of utmost importance to avoid potential collisions for future space missions. The following challenges arise in the orbital object tracking problem:

- The highly *non-linear* nature of the motion models and the presence of a number of external forces, other than gravitational interaction, such as solar drag and third-body perturbations, adds computational complexity to the state propagation models.
- Problem-specific *Initial Orbit Determination (IOD)* is necessary when the measurements of the full state (i.e. both position and velocity) of the object required for propagation are not available.
- Due to the relatively *small observation times* and the limited field of view of a single sensor, the object remains unobserved most of the time.
- The problem of *noise* and *clutter* is common to all tracking problems, however, combined with the previously mentioned issues, tracking RSOs poses more challenges than traditional tracking scenarios.
- The relatively low illumination of debris compared to other objects such as stars or the moon further complicates their detection and code.

In this report, the work carried out during this final period is shown. First, the robust versions of the filter implemented in year 1 for radar data are shown. These extensions do not rely on particular values for the parameters of the detection statistics. Instead, these parameters are incorporated into the filtering process. Second, initial work towards the use of visual data is presented. To this end, a data set obtained at Georgia Institute of Technology, the OmniSSA data set, is used. Initial work using this data set corresponds to the required pre-processing of images, detection of astronomical objects such as stars in order to obtaining the corresponding mapping between image and celestial coordinates.

This report is organized as follows. In Section 3 a description of the radar data set used to evaluate the proposed robust filtering algorithms and the visual data set used to evaluate detection methods are shown. Section 4 presents the robust extensions to the standard JoTT filter in order to be less dependent on particular values of the detection statistics' parameters. Then, in Section 5 the initial procedures are carried out using the visual data set are described. Section 6 shows the results of the newly proposed filtering algorithms and of the initial procedures performed in the visual data, and finally in Section 7 possible future work is discussed.

2 Project Outreach

This project has resulted in two published articles, one conditionally accepted publication, and one workshop presentation as follows:

- ISI Journal Article: *"Robust Joint Target Detection and Tracking for Space Situational Awareness"*, Andrey Pak, Javier Correa and Martin Adams, AIAA Journal of Guidance, Control, and Dynamics, Conditionally Accepted for publication.
- ISI Journal Article: *"Metrics for Evaluating Feature-Based Mapping Performance"*, Pablo Barrios, Martin Adams, Keith Leung, Felipe Inostroza, Ghayur Naqvi, Marcos E. Orchard, IEEE Transactions on Robotics, Vol. 33, Issue 1, pages 198 to 213, Feb. 2017.

- Conference Article: *"Estimating Detection Statistics within a Bayes-Closed Multi-Object Filter"*, Javier Correa, Martin Adams, 19th International Conference on Information Fusion (FUSION), July, 2016.
- SSA2016 Workshop on Space Situational Awareness, La Serena, Chile, April 2016. Presentation title: *"Joint Object Detection and Tracking Filter for Chilbolton Advanced Meteorological Radar Data Processing"*.

3 Datasets

In this section, a brief description of the data sets used is provided.

3.1 CAMRa Radar Data sets

Two types of data sets were obtained from CAMRa: raw and post-processed. For each data acquisition step, the whole A-scope of a radar, namely the function of returned signal intensity over the range, is recorded and stored in a raw (netCDF) file, which is typical for an atmospheric radar. Each A-scope contains 27,000 75-m bins for returned co-polar and cross-polar signal strength. The size of a raw data file averages at 2 Gb per observation. For size considerations, the raw data is post-processed, leaving one detection per time step, associated with the strongest returned signal strength. For a more detailed explanation of the CAMRa the viewer is referred to [5].

3.2 The OmniSSA Visual Data set

This OmniSSA data sets consist of images taken from three identical SR cameras positioned equidistantly. The camera resolution is 3326×2054 pixels, the field of view is $66^\circ \times 82^\circ$. The three cameras take the pictures simultaneously, and their calibration parameters using the Brown distortion model [6] are included. The data set is composed of observations made during one night in Atlanta (33.777468° N, 84.398969° W) and it contains 27 images per camera in the Flexible Image Transport System (FITS) format. The images were taken at different exposition times, the first 1 sec., thee of them 15 sec., and the rest 30 sec. The database was provided by Dr. Marcus Holzinger from Georgia Institute of Technology. Further details about the data set can be found in [7].

Figure 1 shows the sampling times of the data set. The vertical axis is the label of the image. The horizontal axis is the time the photographs were taken, while the length of the line represents its exposition time. Figure 1b shows a subsampling between images 7 to 11. Figures show that the sample time is irregular, and at the best case the same object (satellite) appears in two following images. For this reason, this data set cannot be used for tracking, but other tasks can be done, like object detection or coordinate mapping (conversion from image pixels to celestial coordinates and vice versa).

4 Radar-based Tracking

In this section, methods two methods for processing the data generated by the radar-based tracker are presented. For a detailed explanation, please refer to the attached article.

4.1 Constant False Alarm Rate (CFAR) Processor

The original detection extraction algorithm in CAMRa measurement processing was using the range bin corresponding to the strongest signal strength. This method could fail to detect a valid target in the presence of occludents, transient objects or high intensity noise. A more robust method of line of sight peak detection is the CFAR family of algorithms [1]. The family of CFAR algorithms are based on local statistics estimation to estimate peaks within the received radar signal. In particular, the CA-CFAR algorithm, diagrammatically shown in Figure 2, is evaluated in this report. The CA-CFAR algorithm

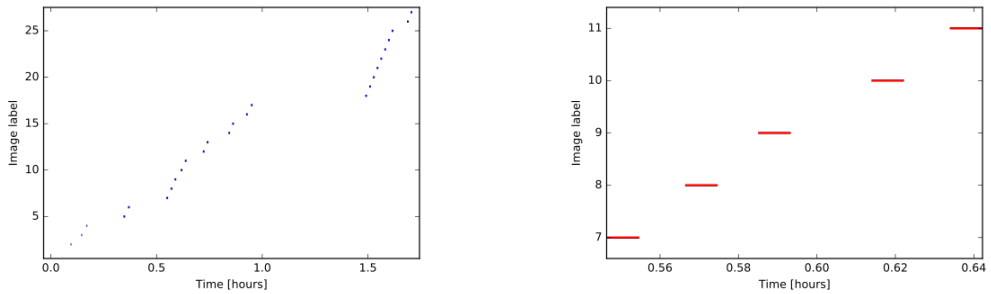

(a) All images (b) Images 7-11

Figure 1: Sample times of the data set

can be described as a sliding window operator around the current cell that evaluates its neighborhood to determine the local threshold. If the current cell being evaluated is above the local threshold, it is reported as a peak. Since this method works on local basis, it can report more than one peak per radar scan.

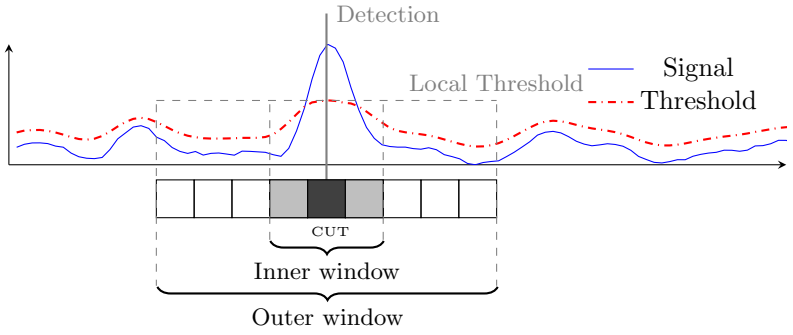

Figure 2: An example of theCA-CFAR operation. The neighborhood of the current cell under test (CUT) is evaluated to estimate an appropriate detection threshold. The black square designates the CUT and the corresponding guard cells are shown in Grey.

4.2 Gaussian Mixture Joint Target Detection and Tracking Filter

For the original analytical explanation of the JoTT filter the reader is referred to [21, 12, 16].

The JoTT filter is a RFS-based filter designed to estimate a single track when multiple measurements are received. To do so, the presence of an object and its state is modeled as a Bernoulli RFS:

$$X \sim \text{Bernoulli RFS}\,(q, s) \equiv f_{\text{Bernoulli}}(X) = \begin{cases} 1-q, & \text{if } X = \emptyset \\ qs(\mathbf{x}), & \text{if } X = \{\mathbf{x}\} \\ 0, & \text{otherwise,} \end{cases} \tag{1}$$

with X being a random set that can one zero element with probability $1-q$ and exactly one element with probability q.

Analogous to standard vector-based filtering, a set-transition model is required. A standard, or "natural", transition model for an RFS state is shown in Figure 3 and defined as:

- If no target is present, one can be born with probability P_B, and distributed according to $f_B(\cdot)$. Conversely, if no target is present, there will be no target with probability $1-P_B$. These cases are shown in Figure 3a.

- If a target is present in the environment, the target survives with probability $P_S(\mathbf{x})$ and its state evolves in time according to $f_{k|k-1}(\cdot|\cdot)$. If a target is present, it will cease to exists with probability $1 - P_S$. These cases are shown in Figure 3b.

Using this description, the pdf for the transition RFS $P(X_k|X_{k-1})$ can be expressed as follows:

$$P(X_k|X_{k-1}) = \begin{cases} \text{Bernoulli RFS}\left(P_S(\mathbf{x}_{k-1}), f_{k|k-1}(\cdot|\mathbf{x}_{k-1})\right), & \text{if } X_{k-1} = \{\mathbf{x}_{k-1}\} \\ \text{Bernoulli RFS}\left(P_B, f_B\right), & \text{if } X_{k-1} = \emptyset, \end{cases}, \tag{2}$$

where $P_S(\mathbf{x})$ is the probability of survival of a target located at $\mathbf{x}$, $f_{k|k-1}(\mathbf{x}_k|\mathbf{x}_{k-1})$ is the prediction model for a target located at $\mathbf{x}_{k-1}$, P_B is the probability of the target appearing in the environment and $f_B(\mathbf{x})$ is the spatial distribution of the newly born target.

Now, assuming that $P(X_{k-1}|Z_{1:k-1})$ is Bernoulli distributed - i.e. Bernoulli RFS(q_{k-1}, s_{k-1}), it is possible to show that the predicted RFS, $P(X_k|Z_{1:k-1})$, is also a Bernoulli RFS [12, Section 14.7.3] with parameters:

$$q_{k|k-1} = (1 - q_{k-1})P_B + q_{k-1}P_S \tag{3}$$

$$s_{k|k-1}(\mathbf{x}_k) = \frac{(1 - q_{k-1})P_B f_B(\mathbf{x}_k) + q_{k-1}P_S(\mathbf{x}_k) \int f_{k|k-1}(\mathbf{x}_k|\mathbf{x}_{k-1}) s_{k-1}(\mathbf{x}_{k-1}) d\mathbf{x}_{k-1}}{q_{k|k-1}}. \tag{4}$$

The predicted RFS, can be corrected with the received set-based measurements using Bayes theorem to obtain the required estimated posterior RFS. To achieve this, first a model of the measurements is required. Similar to the standard multi-target model, the standard multi-target detection model, shown in Figure 4, is defined as:

1. Received measurements, shown as squares in Figure 4, are either clutter or a single measurement resulting from the target, shown as circles in Figure 4.

2. If a target is present in the environment, it generates a measurement with probability $P_D(\mathbf{x})$ which is distributed according to $f_z(\mathbf{z}|\mathbf{x})$. This case is shown in Figure 4a.

3. Clutter measurements are statistically independent of the target.

This model can be interpreted as the union of two sets,

$$Z = \Theta \cup Z|X, \tag{5}$$

namely the set of clutter measurements Θ and the set with the valid measurement generated by the target $Z|X$. A standard model for the clutter RFS Θ is the Poisson RFS with parameters λ_Θ for the clutter rate and $\kappa(\mathbf{z})$ for the spatial distribution of the clutter measurements, as shown in Figure 4b. In a

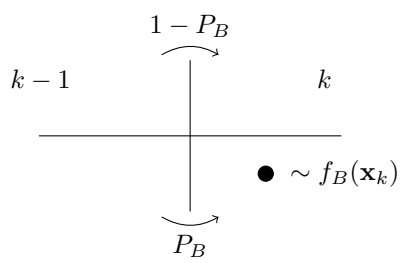

(a) Transition model for $X_{k-1} = \emptyset$

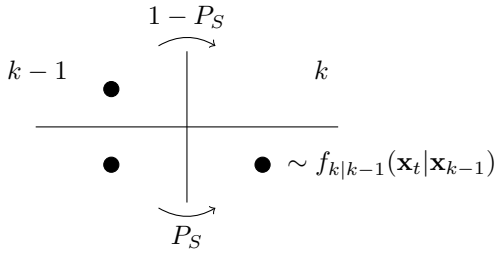

(b) Transition model for $X_{k-1} = \{\mathbf{x}_{k-1}\}$

Figure 3: Graphical representation of the standard RFS transition model.

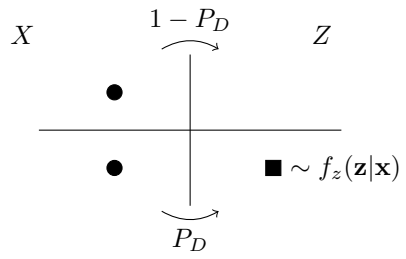

(a) Observation model for the target X

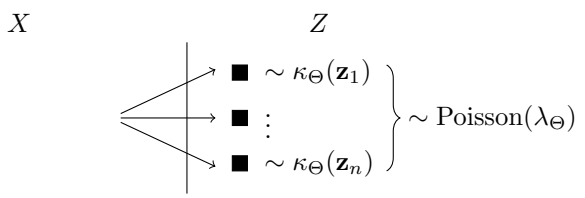

(b) Observation model for clutter measurements

Figure 4: Graphical representation of the standard RFS detection model.

Poisson RFS the number of elements of the set is Poisson distributed, while the elements are identically and independently distributed according to the spatial distribution.

Following the description of the standard multi-target measurement model, the model for the measurement resulting from the target can be written as:

$$P(Z|X) = \begin{cases} \text{Bernoulli RFS}(P_D(\mathbf{x}), f_z(\mathbf{z}|\mathbf{x})), & \text{if } X = \{\mathbf{x}\} \\ 0, & \text{otherwise} \end{cases}, \tag{6}$$

where $f_z(\mathbf{z}|\mathbf{x})$ is the likelihood of observing $\mathbf{z}$ from target state $\mathbf{x}$ and $P_D(\mathbf{x})$ is the probability of detecting a target located at $\mathbf{x}$.

It is possible to show that, using the standard multi-target likelihood, if the prior distribution is distributed as Bernoulli RFS $(q_{k|k-1}, f_{k|k-1})$ then the posterior distribution is also a Bernoulli RFS [12, Section 14.7.4] now with parameters:

$$q_k = q_{k|k-1} \frac{\int (1 - P_D(\mathbf{x}))s_{k|k-1}(\mathbf{x}) + \sum_{\mathbf{z}\in Z_k} \frac{P_D(\mathbf{x}) f_z(\mathbf{z}|\mathbf{x}) s_{k|k-1}(\mathbf{x})}{\lambda_\Theta \kappa(\mathbf{z})} d\mathbf{x}}{1 - q_{k|k-1} + q_{k|k-1} \left(\int (1 - P_D(\mathbf{x}))s_{k|k-1}(\mathbf{x}) + \sum_{\mathbf{z}\in Z} \frac{P_D(\mathbf{x}) f_z(\mathbf{z}|\mathbf{x}) s_{k|k-1}(\mathbf{x})}{\lambda_\Theta \kappa(\mathbf{z})} d\mathbf{x} \right)} \tag{7}$$

$$s_k(\mathbf{x}) = \frac{1}{q_k} \left((1 - P_D(\mathbf{x}))s_{k|k-1}(\mathbf{x}) + \sum_{\mathbf{z}\in Z} \frac{P_D(\mathbf{x}) f_z(\mathbf{z}|\mathbf{x}) s_{k|k-1}(\mathbf{x})}{\lambda_\Theta \kappa(\mathbf{z})} \right). \tag{8}$$

An analytic solution for this filter is obtained when the underlying spatial distribution $s(\mathbf{x})$ is assumed to be a Gaussian mixture:

$$s_k(\mathbf{x}) = \sum_{i=1}^{N} w^{(i)} \mathcal{N}(\mathbf{x}, \mathbf{m}^{(i)}, \mathbf{P}^{(i)}). \tag{9}$$

Similarly, the distribution of the locations where the target can appear, is also modeled with a Gaussian mixture:

$$f_B(\mathbf{x}) = \sum_{i=1}^{N} w_B^{(i)} \mathcal{N}(\mathbf{x}, \mathbf{m}_B^{(i)}, \mathbf{P}_B^{(i)}), \tag{10}$$

where $w_B^{(i)}, \mathbf{m}_B^{(i)}$ and $\mathbf{P}_B^{(i)}$ are the weights, means and covariances of the components of the birth process. The the probabilities of survival and detection are constant in this formulation of the filter.

With these assumptions it is possible to show that after the prediction step, the new parameters of

the Bernoulli RFS are:

$$q_{k|k-1} = P_B(1-q_k) + P_S q_k \tag{11}$$

$$s_{k|k-1}(x) = \frac{P_B(1-q_k)}{q_{k|k-1}} f_{B_k}(x) + \frac{P_S q_k}{q_{k|k-1}} \sum_{i=1}^{N_{k-1}} w_{k-1}^{(i)} \mathcal{N}(\mathbf{x}; \mathbf{m}_{k|k-1}^{(i)}; \mathbf{P}_{k|k-1}^{(i)}). \tag{12}$$

The distribution of the components of the mixture are also preserved as Gaussians, with mean $\mathbf{m}_{k|k-1}$ and covariance $\mathbf{P}_{k|k-1}$ corresponding to the regular Kalman filter's or Extended Kalman Filter (EKF)'s prediction equations:

$$\mathbf{m}_{k|k-1} = \mathbf{F}_{k-1}\mathbf{m}_{k-1}^{(i)} \tag{13}$$

$$\mathbf{P}_{k|k-1} = \mathbf{F}_{k-1}\mathbf{P}_{k-1}^{(i)}\mathbf{F}_{k-1}^T + \mathbf{Q}_{k-1}. \tag{14}$$

During the update step of the JoTT filter, the corrected parameters for the Bernoulli RFS are:

$$q_k = \frac{1-\Delta_k}{1-q_{k|k-1}\Delta_k} q_{k|k-1} \tag{15}$$

$$s_k = \frac{1-P_D}{1-\Delta_k} s_{k|k-1}(\mathbf{x}) + \frac{P_D}{1-\Delta_k} \sum_{\mathbf{z}\in Z} \sum_{i=1}^{N_{k-1}} \frac{w_k^{(i)} L_k^{(i)}(z)}{\lambda\kappa(\mathbf{z})} \mathcal{N}(\mathbf{x}; \mathbf{m}_k^{(i)}; \mathbf{P}_k^{(i)}) \tag{16}$$

$$1\Delta_k = P_D \left[1 - \sum_{\mathbf{z}\in Z} \sum_{i=1}^{N_{k-1}} \frac{w_k^{(i)} L_k^{(i)}(z)}{\lambda\kappa(\mathbf{z})} \right], \tag{17}$$

where:

$$L_k^{(i)}(\mathbf{z}) = \mathcal{N}(\mathbf{z}; \mathbf{H}_k\mathbf{m}_{k|k-1}^{(i)}; \mathbf{H}_k\mathbf{P}_{k|k-1}^{(i)}\mathbf{H}_k^T + \mathbf{R}_k) \tag{18}$$

$$\mathbf{K}_k = \mathbf{P}_{k|k-1}^{(i)}\mathbf{H}_k^T + \mathbf{R}_k \tag{19}$$

$$\mathbf{m}_k = \mathbf{m}_{k|k-1} + \mathbf{K}_k^{(i)}(\mathbf{z} - \mathbf{H}_k\mathbf{m}_{k|k-1}^{(i)}) \tag{20}$$

$$\mathbf{P}_k = (\mathbf{I} - \mathbf{K}_k\mathbf{H}_k)\mathbf{P}_{k|k-1}. \tag{21}$$

4.3 Robust Versions of the JoTT Filter

The standard JoTT filter, requires the parameters for the detection statistics to be specified a priori, namely the probability of detecting the target and the rate at which clutter is detected and how it is distributed spatially. These parameters are non-trivial to describe in terms of a theoretical analysis of the sensor or to estimate in an off-line process, since the detection statistics are likely to vary in time. To overcome this issue, two extensions to the JoTT filter were developed which are capable of jointly estimating the presence or absence of, and the distribution of a target and the probability of detection and clutter rate.

4.3.1 JoTT filter with unknown P_D

In the formulation of the JoTT filter, it was assumed that the probability of detection was state dependent. This suggests that we could extend our state space to directly include the probability of detection as one its values,

$$\hat{\mathbf{x}} = [\mathbf{x}, P_D]. \tag{22}$$

Given that a model for the distribution of P_D is provided, this simple extension allows the filter to include the estimation of P_D at a very low cost.

To account for a possibly unknown and time varying P_D, a βGM was used in [13] as a variation of a Gaussian Mixture for the P_D-Probability Hypothesis Density (PHD) and P_D-Cardinalized Probability Hypothesis Density (CPHD) filters.

The appearance or disappearance of the target in the environment can be seen as a Bernoulli experiment, and a natural model for the parameter of a Bernoulli distribution, in this case the probability of detection, is a Beta distribution [4, Section 8.2]. As such, and similar to the standard JoTT filter, an analytical solution is obtained assuming that the distribution of the new state shown in Equation 22 is now a Beta-Gaussian mixture.

The prediction step for the probability of target existence and the spatial distribution is similar to the standard JoTT filter. They differ in that the spatial birth distribution has to have Beta components along with the Gaussian component:

$$f_B(\mathbf{x}) = \sum_{i=1}^{N} w_B^{(i)} \mathcal{N}(\mathbf{x}, \mathbf{m}_B^{(i)}, \mathbf{P}_B^{(i)}) \operatorname{Beta}(P_D, a_B^{(i)}, b_B^{(i)}). \tag{23}$$

The prediction model for the Beta assumes that the probability of detection follows a random walk. In practice this is implemented by, at the prediction step, maintaining the expected value and increasing the variance by a small amount. This avoids the problem of the Beta components converging to a highly concentrated point, and allows the incorporation of temporal variability. This is achieved by multiplying both parameters of the Beta distribution by a constant value, resulting in the maintenance of the expected value, but an increase in the variance by a value ϵ. The multiplicative constant can be estimated from:

$$\sigma^{2\ (i)}_{B,k|k-1} = \sigma^{2\ (i)}_{B,k-1} + \epsilon. \tag{24}$$

This results in the following parameters for the predicted Beta components

$$\theta^{(i)} = \frac{a_{k-1}^{(i)} b_{k-1}^{(i)} - \epsilon \left(a_{k-1}^{(i)} + b_{k-1}^{(i)}\right)^2}{\epsilon \left(a_{k-1}^{(i)} + b_{k-1}^{(i)}\right)^3} \tag{25}$$

$$a_{k|k-1}^{(i)} = \theta^{(i)} a_{k-1}^{(i)} \tag{26}$$

$$b_{k|k-1}^{(i)} = \theta^{(i)} b_{k-1}^{(i)}. \tag{27}$$

Once the predicted distribution is obtained, the βGM-JoTT update resembles the JoTT update with the slight difference that each instance of the P_D term, which appears in the original JoTT filter, is replaced by $\frac{a_{k|k-1}^{(i)}}{a_{k|k-1}^{(i)}+b_{k|k-1}^{(i)}}$. Conversely, each instance of the term $(1-P_D)$ is replaced by $\frac{b_{k|k-1}^{(i)}}{a_{k|k-1}^{(i)}+b_{k|k-1}^{(i)}}$. This results in Equation 16 being replaced by

$$\begin{aligned} s_k([\mathbf{x}, P_D]) = {} & \frac{1}{1-\Delta_k} \sum_{i=1}^{N_{k|k-1}} w_{k|k-1} \frac{b_{k|k-1}^{(i)}}{a_{k|k-1}^{(i)} + b_{k|k-1}^{(i)}} \mathcal{N}(\mathbf{x}; \mathbf{m}_{k|k-1}^{(i)}; \mathbf{P}_{k|k-1}^{(i)}) \operatorname{Beta}(P_D, a_{M,k}^{(i)}, b_{M,k}^{(i)}) \\ & + \frac{1}{1-\Delta_k} \sum_{\mathbf{z}\in Z} \sum_{i=1}^{N_{k|k-1}} w_k^{(i)} \frac{a_{k|k-1}^{(i)}}{a_{k|k-1}^{(i)} + b_{k|k-1}^{(i)}} \frac{L_k^{(i)}(z)}{\lambda \kappa(\mathbf{z})} \mathcal{N}(\mathbf{x}; \mathbf{m}_k^{(i)}; \mathbf{P}_k^{(i)}) \operatorname{Beta}(P_D, a_{D,k}^{(i)}, b_{D,k}^{(i)}), \end{aligned} \tag{28}$$

with the new Beta components (assuming $i = 1 \dots N_{k|k-1}$ and $j = 1 \dots |Z|$)

$$\begin{array}{llll} a_{M,k}^{(i)} & = a_{k|k-1}^{(i)}, & b_{M,k}^{(i)} & = b_{k|k-1}^{(i)} + 1 \\ a_{D,k}^{(N_{k|k-1}+ij)} & = a_{k|k-1}^{(i)} + 1, & b_{D,k}^{(N_{k|k-1}+ij)} & = b_{k|k-1}^{(i)}. \end{array}$$

4.3.2 JoTT filter with unknown detection statistics

The formulation presented in the previous section has its limitations. For example, it is not possible to extend the state space to account for clutter, since in the derivation of the JoTT filter, clutter and targets are assumed independent from one another, and thus the clutter parameter would be unobserved.

To estimate the clutter process, Mahler [13, Section 18.3] used the idea of clutter generators. Clutter generators are analogous to targets, but generate clutter measurements only. By applying this model to the JoTT filter, it would convert a single-target filter, into a multi-target filter, as it would be required to keep track of the object of interest as well as the possible multiple clutter generators. A different approach is used in this work, where a standard Poisson model is assumed for the clutter process, but with an unknown, and possibly time-varying, clutter rate parameter. The problem then becomes how to model and estimate the clutter rate parameter.

To derive a JoTT filter robust to both, unknown probability of detection P_D and clutter rate λ_Θ, a full probabilistic re-formulation is required. Instead of extending the state space, both these statistics are incorporated into the estimation problem. Thus, the values which must be estimated are the Bernoulli set X corresponding to the estimated target, the probability of detection P_D and the rate at which clutter appears in the sensor data λ_Θ, resulting in a joint probability distribution

$$P(X_k, P_{D_k}, \lambda_{\Theta_k} | Z_{1:k}), \tag{29}$$

with X_k being the set representation of the target (empty or single element set), P_{D_k} is the probability of detection and λ_{Θ_k} is the clutter rate at time step k.

This model has a secondary advantage. Since the value for P_D does not depend on the estimated state, it is now theoretically possible to obtain and estimate P_D even when no target is present in the environment (e.g. $q = 0$). This helps in the (re-)initialization of targets when there has been a long period of only clutter measurements.

It is assumed that the joint probability distribution in (29) has the following form:

$$P(X_k, P_{D_k}, \lambda_{\Theta_k} | Z_{1:k}) = \begin{cases} \sum_{j=1}^{m} w_{\emptyset,k}^{(j)} G_{\emptyset,k}^{(j)} B_{\emptyset,k}^{(j)} & , \text{ if } X = \emptyset \\ \sum_{i=1}^{n} w_{X,k}^{(i)} G_{X,k}^{(i)} B_{X,k}^{(i)} s_{X,k}^{(i)} & , \text{ if } X = \{\mathbf{x}\} \\ 0 & , \text{otherwise,} \end{cases}, \tag{30}$$

with $G_{\square,k}^{(\ell)} = G_{\square,k}^{(\ell)}(\lambda_\Theta), B_{\square,k}^{(\ell)} = B_{\square,k}^{(\ell)}(P_D)$ and $s_{\square,k}^{(\ell)} = s_{\square,k}^{(\ell)}(\mathbf{x})$ being the distributions for the clutter rate, probability of detection and the target's spatial distribution respectively, and $w_{\square,k}^{(\ell)}$ the weights such that $\sum_{j=1}^{m} w_{\emptyset,k}^{(j)} + \sum_{i=1}^{n} w_{X,k}^{(i)} = 1$. The square symbol can be either $\square = \emptyset$, belonging to the mixture representing target non-existence, or $\square = X$, indicating target existence in Equation (30). The arguments of the functions $G_{\square,k}^{(k)}, B_{\square,k}^{(k)}$ and s_k will be omitted when possible for a clearer exposition. For a fully robust filter, with unknown detection statistics, the complexity of the formulation of the filter increases considerably. Intuitively, the probability of a target being present in the environment is now $q = \sum_{i=1}^{n} w_{X,k}^{(i)}$, while the probability of no target being present is $1 - q = \sum_{j=1}^{m} w_{\emptyset,k}^{(j)}$.

Assuming that the number of clutter measurements is Poisson distributed, a natural distribution to model the rate of clutter is the Gamma distribution [4, Section 10.1]. As such, a Gamma distribution is adopted to model the clutter rate,

$$G_{\square,k}^{(\ell)}(\lambda_\Theta) = \text{Gamma}(\lambda_\Theta, \alpha_{\square,k}^{(\ell)}, \beta_{\square,k}^{(\ell)}) = \frac{{\beta_{\square,k}^{(\ell)}}^{\alpha_{\square,k}^{(\ell)}}}{\Gamma(\alpha_{\square,k}^{(\ell)})} \lambda_\Theta^{\alpha_{\square,k}^{(\ell)}-1} e^{-\beta_{\square,k}^{(\ell)} \lambda_\Theta}, \tag{31}$$

where $\alpha_{\square,k}^{(\ell)}$ and $\beta_{\square,k}^{(\ell)}$ are the parameters of the Gamma distribution, and a Beta distribution to model the detection probability,

$$B_{\square,k}^{(\ell)}(P_D) = \text{Beta}(P_D, a_{\square,k}^{(\ell)}, b_{\square,k}^{(\ell)}) = \frac{P_D^{a_{\square,k}^{(\ell)}-1} (1 - P_D)^{b_{\square,k}^{(\ell)}-1}}{\beta(a_{\square,k}^{(\ell)}, b_{\square,k}^{(\ell)})}, \tag{32}$$

with $a^{(\ell)}_{\square,k}$ and $b^{(\ell)}_{\square,k}$ being the parameters of the Beta distribution.

At the prediction step, assuming that the distribution at time $k-1$ is of the form of Equation (30), it is possible to show that the predictive distribution has the same form:

$$P(X_{k|k-1}, P_{D_{k|k-1}}, \lambda_{\Theta_{k|k-1}}|Z_{1:k-1}) = \begin{cases} \sum_{j=1} w^{(j)}_{\emptyset,k|k-1} G^{(j)}_{\emptyset,k|k-1} B^{(j)}_{\emptyset,k|k-1} & , \text{ if } X_{k|k-1} = \emptyset \\ \sum_{i=1} w^{(i)}_{X,k|k-1} G^{(i)}_{X,k|k-1} B^{(i)}_{X,k|k-1} s^{(i)}_{X,k|k-1} & , \text{ if } X = \{\mathbf{x}\}, \end{cases} \tag{33}$$

where for the first m elements of the mixture ($i = 1 \dots m$)

$$w^{(i)}_{X,k|k-1} = w^{(i)}_{\emptyset,k-1} P_B, w^{(i)}_{\emptyset,k|k-1} = w^{(i)}_{\emptyset,k-1}(1 - P_B), \tag{34}$$

$$G^{(i)}_{X,k|k-1} = G^{(i)}_{\emptyset,k-1}, G^{(i)}_{\emptyset,k|k-1} = G^{(i)}_{\emptyset,k-1}, \tag{35}$$

$$B^{(i)}_{X,k|k-1} = B^{(i)}_{\emptyset,k-1}, B^{(i)}_{\emptyset,k|k-1} = B^{(i)}_{\emptyset,k-1}, \tag{36}$$

$$s^{(i)}_{X,k|k-1} = f_B, \tag{37}$$

and for the last n elements

$$w^{(i+m)}_{X,k|k-1} = w^{(i)}_{X,k-1} \tau_i, w^{(i+m)}_{\emptyset,k|k-1} = w^{(i)}_{X,k-1}(1 - P_S), \tag{38}$$

$$G^{(i)}_{X,k|k-1} = G^{(i)}_{X,k-1}, G^{(i+m)}_{\emptyset,k|k-1} = G^{(i)}_{X,k-1}, \tag{39}$$

$$B^{(i+m)}_{X,k|k-1} = B^{(i)}_{X,k-1}, B^{(i+m)}_{\emptyset,k|k-1} = B^{(i)}_{X,k-1}, \tag{40}$$

$$s^{(i+m)}_{X,k|k-1} = \frac{1}{\tau_i} \int P_S(\mathbf{x}_{k-1}) f_{k|k-1}(\mathbf{x}_{k|k-1}|\mathbf{x}_{k-1}) s^{(i)}_{X,k-1}(\mathbf{x}_{k-1}) d\mathbf{x}_{k-1}, \tag{41}$$

and τ_i is a normalization constant calculated as follows

$$\tau_i = \iint P_S(\mathbf{x}_{k-1}) f_{k|k-1}(\mathbf{x}_{k|k-1}|\mathbf{x}_{k-1}) s^{(i)}_{X,k}(\mathbf{x}_{k-1}) d\mathbf{x}_{k-1} d\mathbf{x}_k. \tag{42}$$

Note that the parameters related to the clutter and probability of detection, under this model, should remain constant. Similar to the βGM-JoTT filter, to avoid overconfidence and allow a small time variation, a random walk is used to model the evolution of both the clutter rate and probability of detection.

For a clearer exposition, we will assume a constant probability of survival, $P_S(\cdot) = P_S$, which then results in

$$\tau_i = P_S \tag{43}$$

$$s^{(i)}_{X,k}(\mathbf{x}_{k|k-1}) = \int f_{k|k-1}(\mathbf{x}_{k|k-1}|\mathbf{x}_{k-1}) s^{(i)}_{X,k-1}(\mathbf{x}_{k-1}) d\mathbf{x}_{k-1}. \tag{44}$$

To account for the observation at the current time step, if the prior distribution is assumed to be of the form shown in Equation (30), by using Bayes theorem with the standard multi-target likelihood it can also be shown that the corrected (or posterior) probability distribution has the same form

$$P(X_k, P_{D_k}, \lambda_{\Theta_k}|Z_{1:k}) = \begin{cases} \sum_{j=1}^{n} w^{(j)}_{\emptyset,k} G^{(j)}_{\emptyset,k} B^{(j)}_{\emptyset,k} & , \text{ if } X_k = \emptyset \\ \sum_{i=1}^{m(1+|Z|)} w^{(i)}_{X,k} G^{(i)}_{X,k} B^{(i)}_{X,k} s^{(i)}_{X,k} & , \text{ if } X_k = \{\mathbf{x}\}, \end{cases} \tag{45}$$

where, for the case of $X_k = \emptyset$, the parameters of the mixture are

$$w^{(j)}_{\emptyset,k} = w^{(j)}_{\emptyset,k|k-1} \frac{\Gamma\left(\alpha^{(j)}_{\emptyset,k|k-1} + |Z|\right) \beta^{(j)}_{\emptyset,k|k-1}{}^{\alpha^{(j)}_{\emptyset,k|k-1}}}{\Gamma\left(\alpha^{(j)}_{\emptyset,k|k-1}\right) \left(\beta^{(j)}_{\emptyset,k|k-1} + 1\right)^{\alpha^{(j)}_{\emptyset,k|k-1} + |Z|}}, \tag{46}$$

$$\alpha^{(j)}_{\emptyset,k} = \alpha^{(j)}_{\emptyset,k|k-1} + |Z|, \beta^{(j)}_{\emptyset,k} = \beta^{(j)}_{\emptyset,k|k-1} + 1, \tag{47}$$

and the parameters of the Beta component $B^{(j)}_{\emptyset,k}$ are the same as the $B^{(j)}_{\emptyset,k-1}$. Now, for the mixture in the case of $X_k = \{\mathbf{x}\}$, we have m components, related to miss-detecting the target, with parameters

$$w^{(i)}_{X,k} = w^{(i)}_{X,k|k-1} \frac{b^{(i)}_{X,k|k-1}}{a^{(i)}_{X,k|k-1} + b^{(i)}_{X,k|k-1}} \frac{\Gamma\left(\alpha^{(i)}_{X,k|k-1} + |Z|\right) \beta^{(i)}_{X,k|k-1}{}^{\alpha^{(i)}_{X,k|k-1}}}{\Gamma\left(\alpha^{(i)}_{X,k|k-1}\right) \left(\beta^{(i)}_{X,k|k-1} + 1\right)^{\alpha^{(i)}_{X,k|k-1}+|Z|}}, \tag{48}$$

$$\alpha^{(i)}_{X,k} = \alpha^{(i)}_{X,k|k-1} + |Z|, \beta^{(i)}_{X,k} = \beta^{(i)}_{X,k|k-1} + 1, \tag{49}$$

$$a^{(i)}_{X,k} = a^{(i)}_{X,k|k-1}, b^{(i)}_{X,k} = b^{(i)}_{X,k|k-1} + 1, \tag{50}$$

and $m|Z|$ components, related to detecting the target, with parameters ($j = 1 \dots m, \ell = 1 \dots |Z|$)

$$w^{(m+j\ell)}_{X,k} = w^{(i)}_{X,k|k-1} \frac{a^{(i)}_{X,k|k-1}}{a^{(i)}_{X,k|k-1} + b^{(i)}_{X,k|k-1}} \frac{L^{(i)}_{X,k}(\mathbf{z}_\ell)}{\kappa(\mathbf{z}_\ell)} \frac{\Gamma\left(\alpha^{(i)}_{X,k|k-1} + |Z| - 1\right) \beta^{(i)}_{X,k|k-1}{}^{\alpha^{(i)}_{X,k|k-1}}}{\Gamma\left(\alpha^{(i)}_{X,k|k-1}\right) \left(\beta^{(i)}_{X,k|k-1} + 1\right)^{\alpha^{(i)}_{X,k|k-1}+|Z|-1}}, \tag{51}$$

$$\alpha^{(m+j\ell)}_{X,k} = \alpha^{(i)}_{X,k|k-1} + |Z| - 1, \beta^{(m+j\ell)}_{X,k} = \beta^{(i)}_{X,k|k-1} + 1, \tag{52}$$

$$a^{(m+j\ell)}_{X,k} = a^{(i)}_{X,k|k-1} + 1, b^{(m+j\ell)}_{X,k} = b^{(i)}_{X,k|k-1}, \tag{53}$$

$$L^{(i)}_{X,k}(\mathbf{z}) = \int f_z(\mathbf{z}|\mathbf{x}) s^{(i)}_{X,k|k-1}(\mathbf{x}) d\mathbf{x}, \tag{54}$$

$$s^{(i)}_{X,k}(\mathbf{x}) = \frac{f_z(\mathbf{z}|\mathbf{x}) s^{(i)}_{X,k|k-1}(\mathbf{x})}{L^{(i)}_{X,k}(\mathbf{z})}. \tag{55}$$

4.4 State and uncertainty propagation.

Each Gaussian component's mean $\mathbf{m}_{k|k-1}$ and covariance $\Sigma_{k|k-1}$ in a mixture is managed using the corresponding Unscented Kalman Filter (UKF) equations [10]. The propagation of the target state and sigma points is performed through the numerical integration of the state vector according to the model where only gravitational interaction between two bodies is taken into account. In this model, the gravitational acceleration a_G is represented as:

$$a_G = -\frac{\mu}{\|\mathbf{p}\|^3}, \tag{56}$$

where μ is the Earth's gravitational constant. The derivative of the state vector $\mathbf{x}$ used in the integration is then:

$$\frac{d}{dt}\mathbf{x} = \begin{bmatrix} x_4 & x_5 & x_6 & \frac{-\mu x_1}{(\sqrt{x_1^2+x_2^2+x_3^2})^3} & \frac{-\mu x_2}{(\sqrt{x_1^2+x_2^2+x_3^2})^3} & \frac{-\mu x_1}{(\sqrt{x_3^2+x_2^2+x_3^2})^3} \end{bmatrix}^T. \tag{57}$$

5 Vision-based Tracking

Initial work has also been carried out using images for detecting and tracking space debris. This section describes the work carried out to analyze the OmniSSA data set in order to detect possible objects of interest. The OmniSSA data set does not contain data for performing tracking, but the images can be used for pre-processing, such as reducing background noise, removing stars and other objects from the image to be analysed, object detection and obtaining a mapping between celestial coordinates and the image pixels.

5.1 Object detection

SExtractor [3] is a widely used software for source extraction from astronomical images. It detects objects such as stars, satellites, galaxies from FITS images. Then it computes photometry[1] from the detected objects and creates a catalog with information including position, dimension, shape and their statistics.

Figure 5 shows a diagram of the main stages that SExtractor performs for building a catalog of objects from an astronomical image. The process starts by estimating the background produced by noise presented in the image. The image is divided in blocks and a local background noise estimate is obtained from each block using an iterative method. For each iteration, the median ($\bar{I}_{block}$) and standard deviation (σ_{block}) of the pixel intensities are computed. Pixel intensities, which differ significantly from the median value, i.e. those that fulfill $|I(x,y) - \bar{I}_{block}| > 3\sigma$ are rejected, and a new iteration starts with the remaining pixels. The variables x and y indicate the pixel position in the image. Iteration stops when no pixels are rejected. The mean of the remaining pixels is considered as the block background value, unless the σ_{block} value changes more than 20%, in which case the field is considered crowded and the mode value is taken instead. After computing the background for all blocks, a median filter is applied over the entire image in order to eliminate possible local extreme intensities produced by bright stars. As the image was divided in blocks, the temporal background image is low-resolution, thus in order to obtain the full-size background image $I_B(x,y)$, a bicubic-spline interpolation is applied to the low-resolution image.

The background-subtracted image $I_F(x,y)$ is the difference between the input image and the background image. There is an option of using a filter in order to smooth $I_F(x,y)$. The image $I_F(x,y)$ is convolved with the filter, helping to improve the detection of faint and extended objects. SExtractor provides four types of filter: Gaussian, Mexican-hat, top-hat and block, all of them normalized and at various sizes, although other filters can be applied [2, 9]. Gaussian ($F_G(x,y)$), top-hat ($F_{th}(x,y)$) and block ($F_b(x,y)$) filters compute a weighted average around the pixel, useful for emphasizing object pixels while reducing the surrounding noise. Mexican-hat ($F_{Mh}(x,y)$) is a passband-filter, which smooths the image, but also emphasizes edges. It is useful in crowded star fields. The filter functions are shown in Equations 58. For $F_{th}(x,y)$, r represents the radius of the "top-hat". σ^2 represents the variance of the Gaussian part of $F_G(x,y)$ and $F_{Mh}(x,y)$.

$$
\begin{aligned}
F_G(x,y) &= \frac{1}{2\pi\sigma^2}\exp\left(-\frac{x^2+y^2}{2\sigma^2}\right), \\
F_{th}(x,y) &= \begin{cases} 1, & \text{if } x^2+y^2 \leqslant r^2, \\ 0, & \text{otherwise.} \end{cases} \\
F_b(x,y) &= 1, \\
F_{Mh}(x,y) &= \frac{1}{\pi\sigma^2}\left(1-\frac{x^2+y^2}{2\sigma^2}\right)\exp\left(-\frac{x^2+y^2}{2\sigma^2}\right).
\end{aligned}
\tag{58}
$$

A threshold (t_h) is applied to the image and those pixels for which $I_F(x,y) > t_h$ are considered to be part of an object. A deblending algorithm is used to split blobs formed by more than one object. For details of the deblending algorithm refer to the manual [2]. The segmented image is denoted $I_S(x,y)$. Finally the catalog of astronomical objects is built by applying photometry to the segmented objects.

Other useful images can be computed by SExtractor, and used for posible future debris detection algorithms, such as a background-subtracted image in which stars are removed ($I_R(x,y)$). For example debris can be identified as straight lines with pixel intensity values higher than the background, but lower than the stars. This occurs because stars produce their own light, whereas orbiting elements do not. In order to get $I_R(x,y)$ from SExtractor, a suitable threshold, higher than the intensity of the debris but lower than stars, must be selected.

The next Section explains how star detection is used to obtain the transformation between image coordinates and celestial coordinates.

[1] Cited from [17]. Photometry is the science of measuring the flux received from celestial objects. It usually refers to measurements of flux over broad wavelength bands of radiation.

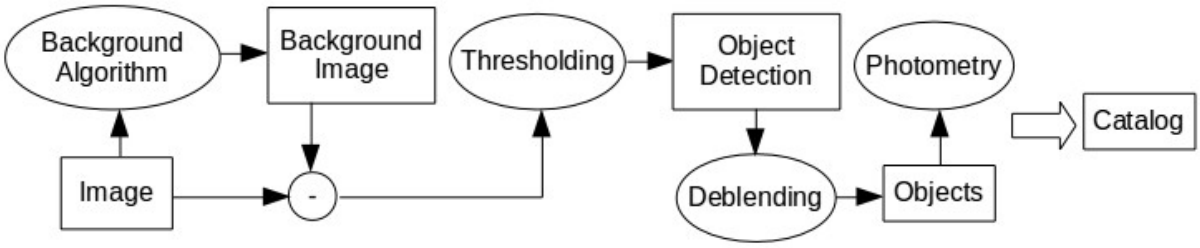

Figure 5: Flow diagram of the most important components of SExtractor showing how it builds a catalog of objects from an astronomical image.

5.2 Coordinate Extraction from the Images

In order to map pixel coordinates from the images to celestial coordinates the SExtractor [3] and Astrometry.net [11] software are used. The first step is to undistort the original images using the provided calibration parameters, then stars and other objects are detected with SExtractor, and finally the detected stars are compared, matched and identified with a catalog of stars. The Tycho-2 catalog [8], provided by Astrometry.net, is chosen for this task because it works better for wide-angle images. The result of the mapping is a polynomial that maps pixels to right ascension and declination from the equatorial celestial coordinates, following the World Coordinate Systems (WCS) standard. The equatorial coordinates given by Astrometry.net are topocentric, and the camera position, latitude and longitude, is needed to obtain the geocentric coordinates.

Debris identification can be carried out by extracting known objects from TLE catalogs. Debris locations are predicted and then projected into the image space using the previously obtained mapping. Details and some examples can be found in the Results section.

6 Results

In this section results of the developed robustified single target multiple measurements filters and of the vision-based detection algorithms are presented. The JoTT filter variants are evaluated on the radar-based CAMRa data set, while the visual detection are evaluated on the OmniSSA data set.

6.1 Radar-Based Results

To evaluate the performance of the proposed extensions to the standard JoTT filter, first, simulations were carried out to then use the real-world CAMRa data set. In the simulated environment, full knowledge of the ground truth is available, thus allowing to accurately measure the estimation errors of the different evaluated approaches.

6.1.1 Simulated Radar Measurement

To show that the proposed filters are robust to unknown and time varying detection statistics, a pass of an orbiting object is simulated. The simulation was created based on the Cosmos-1544 TLE and Simplified General Perturbations - 4 (SGP4) propagation model [19]. The rate at which clutter measurements are generated is arbitrarily assumed to vary sinusoidally with time with values between 4 and 8 clutter measurements per scan, while the probability of detection is arbitrarily assumed to follow a bell-shaped curve, with a minimum value of 5% and a maximum value of 80% as shown in Figure 6. To process this simulated data set, the filters are not provided with the real information related to the detection statistics. For benchmark comparisons, all three filters were executed using the same parameters: probability of survival P_S set to 99.99% and uniform clutter spatial distribution $\kappa(\mathbf{z}) = 25015.77\text{km}^{-3}$. For the standard JoTT filter, P_D was set to 80% and for both, the JoTT and βGM-JoTT filters, λ was set to 4 clutter measurements per time step. The increase in variance for the Beta components of the βGM-JoTT and

r-JoTT filters was set to 10^{-4} per time step and the increase in variance for the Gamma component of the r-JoTT filter was set to 10^{-3} per time step.

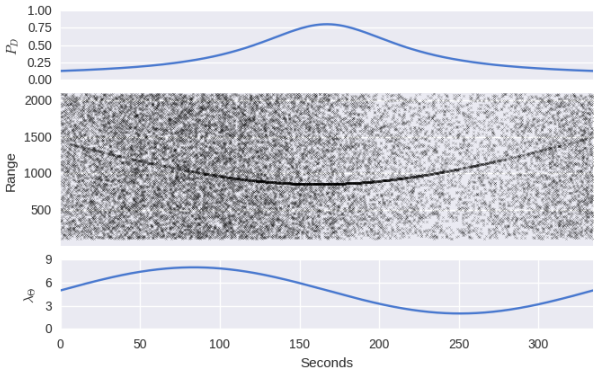

Figure 6: The simulated data set. The upper plot shows the ground truth value for the probability of detection versus time, modeled with a bell-shaped curve, while the lower plot shows the clutter parameter λ which varies sinusoidally with time. The center plot shows the simulated measurements generated using the corresponding detection statistics.

Qualitative results are shown in Figures 7, 8 and 9. It can be seen that in the simulated scenario, the JoTT and βGM-JoTT have some spurious tracks. This is due to the filters removing the existing track, due to the unmatched detection statistics, and creating a new track. This behavior is highlighted by zooming at time steps 0-100, as shown in Figures 7b and 8b.It can be seen that the βGM-JoTT filter suffers less from this problem than the JoTT filter. On the other hand, the r-JoTT does not suffer from this problem as shown in Figure 9. It also has to be noted that the JoTT filter tends to have a large number of discontinuities, as shown in Figure 7b. This is due to the fact that, track continuity, measured by the q value from Equation 1, depends on the value of both the probability of detection P_D and clutter rate λ. Since the JoTT filter assumes fixed values for these parameters, it fails to provide a continuous estimate of the target's existence when parameters don't match the real values. As the βGM-JoTT filter is not dependent on the choice of P_D, it suffers less from this problem and produces a more continuous track (see Figure 8b). The best track is produced by r-JoTT filter as both P_D and λ are estimated.

In Figures 10 and 11, the detection statistic estimates of the βGM-JoTT and r-JoTT filters are shown. It can be appreciated that in all cases the true values are correctly estimated, albeit with small perturbations. The observed jitters on the estimates can be explained as the prediction models for the detection statistic parameters only increase their variance, and no smoothness constraints are assumed.

Quantitative results are shown in Table 1, where the Mean Absolute Error (MAE) between the estimated and the ground truth states is shown in the second column, while in the third column, the percentage of the total simulated time that the filters reported a target is shown. It can be appreciated that the JoTT filter does not perform well in this simulation. This is due to the inability of the JoTT filter to differentiate between dense clutter and the real target when the filter's model of the clutter is incorrect. The βGM-JoTT filter somehow overcomes this problem. This is clearly noted by the fact that the MAE decreases to 4.40km. Clearly the r-JoTT filter outperforms other methods as it is capable of estimating both the clutter density and the probability of detecting a target. It has to be noted that the high MAE values reported by the JoTT and βGM-JoTT filters are mainly due to the estimated false positives.

6.1.2 Results on the CAMRa Data set

In addition to qualitative analysis of the filtering results for the CAMRa data sets, it is possible to compare the performance to the corresponding SGP4 TLE propagation. In order to do so, a historic TLE related to the observation date was retrieved from Spacetrack for the Cosmos-1544 satellite. Superimposed plots

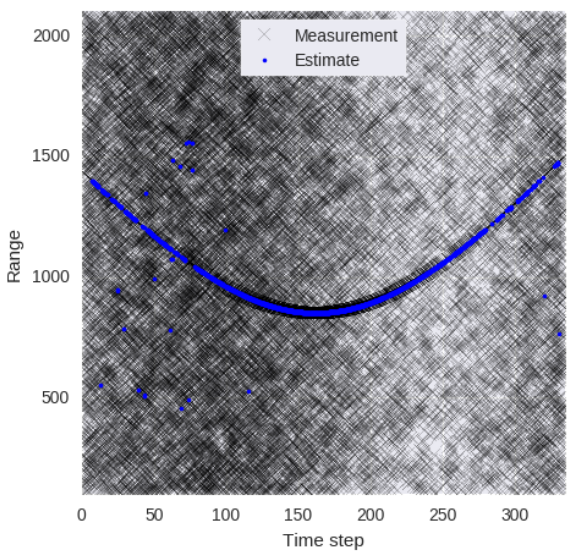

(a) Estimation result using the JoTT filter.

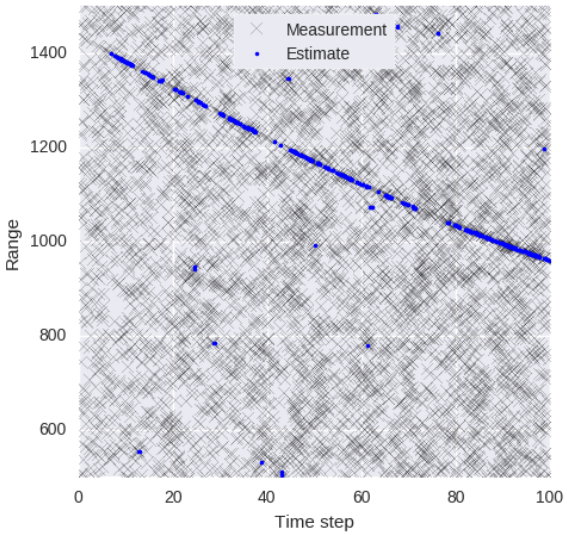

(b) Zoom to the estimate of the JoTT filter between time steps 0 to 100.

Figure 7: Estimated results using the standard JoTT filter.

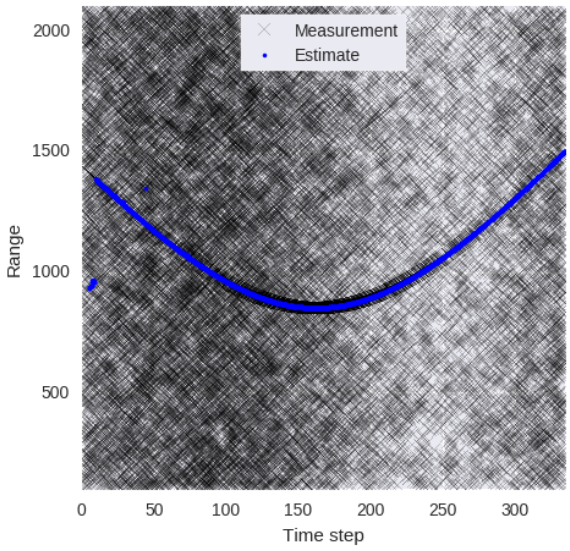

(a) Estimation result using the βGM-JoTT filter.

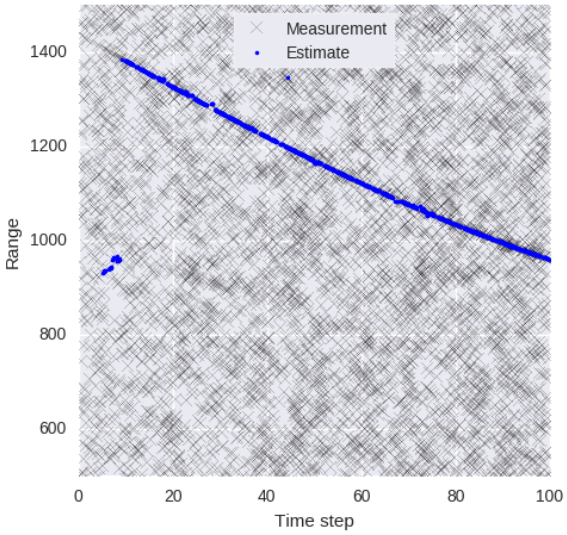

(b) Zoom to the estimate of the βGM-JoTT filter between time steps 0 to 100.

Figure 8: Estimated results using the βGM-JoTT filter.

Method	**MAE**	**% of Time with Est.**
JoTT	6.79 Km	50.66%
βGM-JoTT	4.40 Km	77.29%
r-JoTT	0.08 Km	99.74%

Table 1: Results for the different single tracking approaches. In the first column, the different methods are shown, the second column shows the MAE of the estimate, and in the third column, the percentage of the time a valid estimate is reported by the filter is shown.

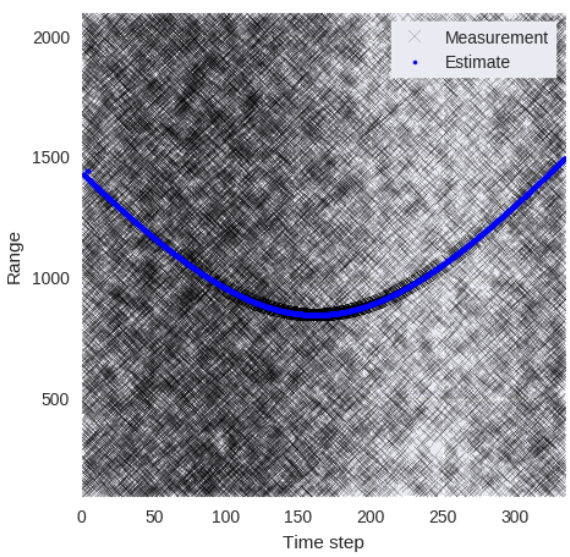

(a) Estimation result using the r-JoTT filter.

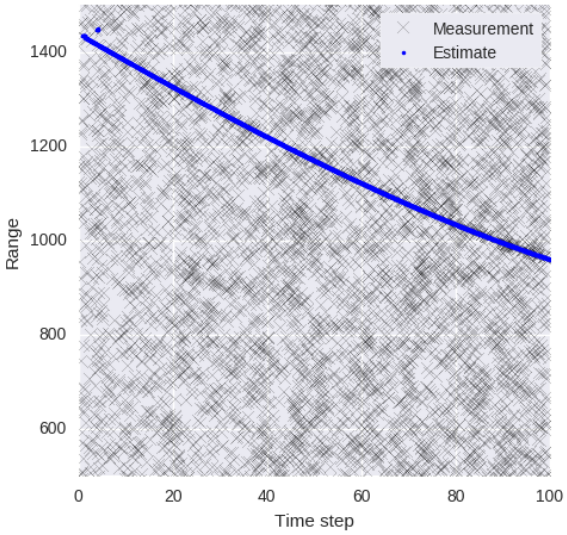

(b) Zoom to the estimate of the r-JoTT filter between time steps 0 to 100.

Figure 9: Estimated results using the r-JoTT filter.

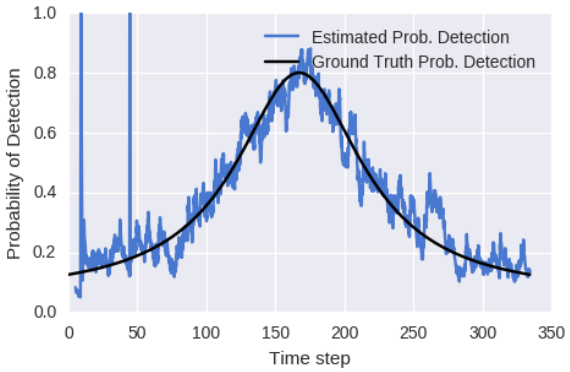

Figure 10: P_D estimate using the βGM-JoTT filter.

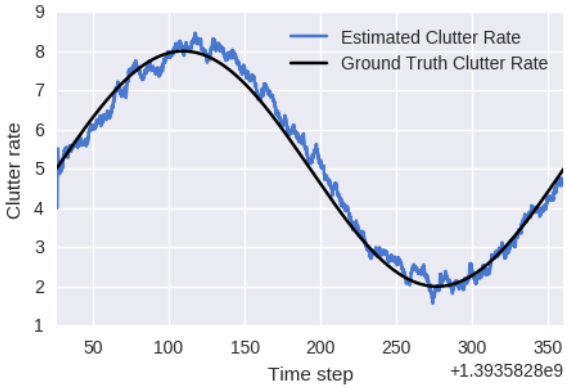

(a) λ estimate using the r-JoTT filter.

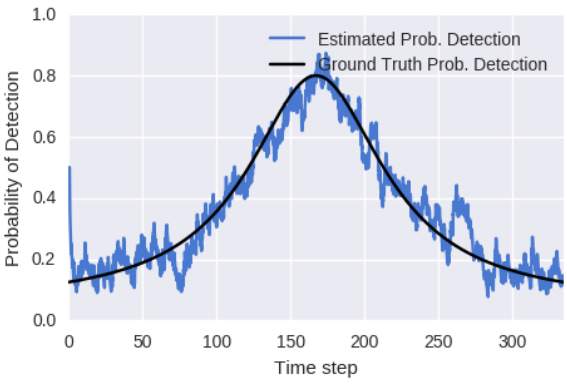

(b) P_D estimate using the r-JoTT filter.

Figure 11: Estimates of the detection statistics for the simulated scenario using the r-JoTT filter.

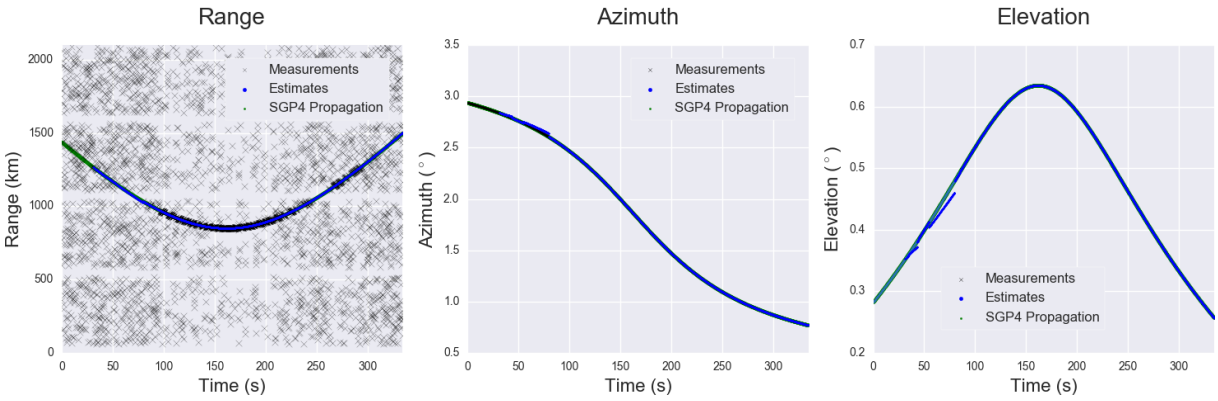

(a) Plots of estimated, measured and propagated range, azimuth and elevation

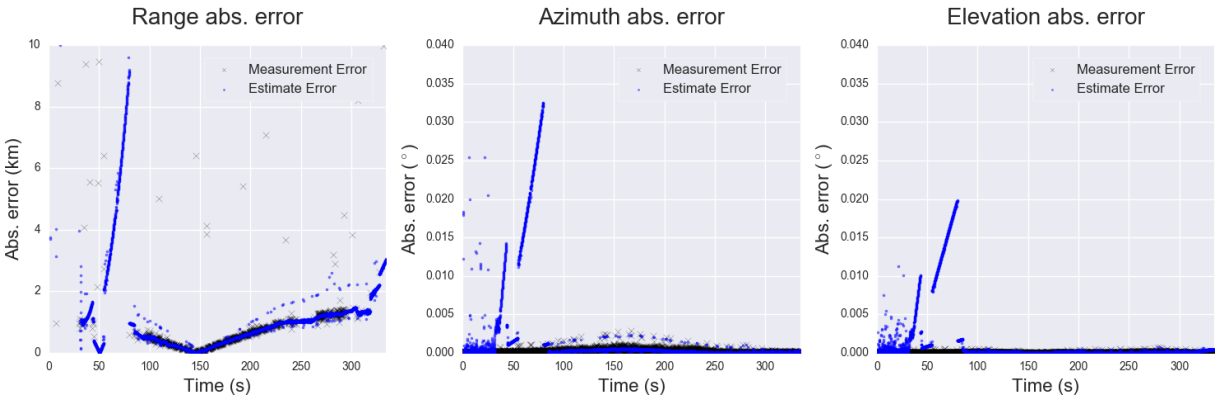

(b) Plots of absolute errors of the estimates and measurements relative to SGP4 propagation.

Figure 12: Comparison of filtering results and SGP4 propagation

of measurements, estimates and propagation as well as estimate errors are shown in Figure 12. The absolute error for azimuth and elevation tends to be zero when the target-generated measurements are present in the scene. This is corroborated by the fact that this particular TLE was used to calculate radar look angels, i.e. aforementioned azimuth and elevation. The same kind of behavior cannot be observed for the range component as it is known that TLE does not provide precise position of the object of interest and the father from epoch it gets, the bigger this position error becomes; thus, this is the main reason why TLE cannot be used to generate reliable ground truth.

Results of analyzing the multiple-measurement CAMRa data sets are shown in Figures 13, 14 and 15. For the single-measurement filtering results please refer to [14].

To test the filter performance in real multiple-measurement scenario, two data sets corresponding to two consecutive passes of the GPM satellite, were chosen. Figure 13 shows the JoTT filter estimates. The parameters used to obtain these result were chosen as follows: probability of detection $P_D = 0.8$, probability of survival $P_S = 1$, and the clutter parameter $\lambda c(z) = \frac{4}{25015.77}$. It has to be noted that the assumed observation volume is uncertain as it is difficult to estimate the real coverage of the radar's beam suitable for filtering. Qualitatively, the results looks a good fit to the data, but for the filter to be confident on the presence of the object it takes approximately 75 time step in Figure 13a and 150 time steps in Figure 13b. In between steps 70 and 100 in Figure 13a the filter leads the estimation to the wrong direction, because the initial estimate obtained after a relatively short target present around step 70 was not precise enough for proper propagation. Visually inspecting the data, it can be appreciated that the target could be tracked much earlier. For the second data set, the qualitative results are noticeably better with the filter being able to distinguish strong clutter close to the end of observation (bottom right corner

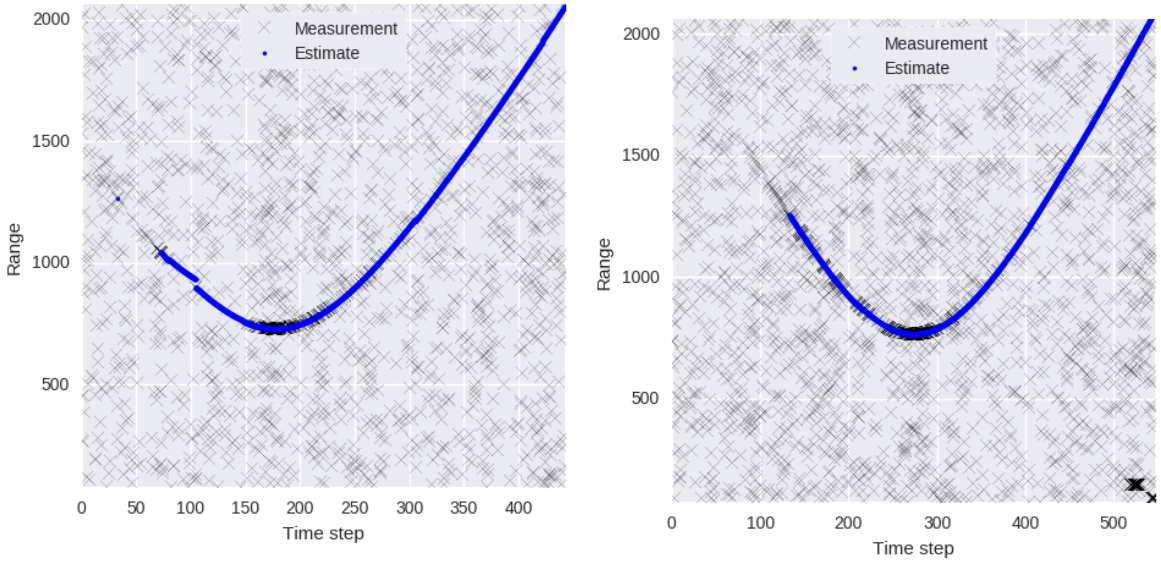

(a) Gaussian mixture (GM)-JoTT filter estimates for the Global Precipitation Measurement (GPM) satellite pass (I).

(b) GM-JoTT filter estimates for the GPM satellite pass (II).

Figure 13: Results of real-world multiple-measurement CAMRa data sets using the standard JoTT filter.

of Fig.Figure 13b).

Figure 14 shows the probability of detection and range estimated by the βGM-JoTT filter. It can now be appreciated that the filter does manage to be confident to have an estimate much earlier compared to the standard JoTT filter as well as avoid the wrong estimation in the beginning of observations approximately between time steps 70 and 100. The probability of detection estimates shown in the upper plots of Figure 14 can be observed to correlate with the presence of target-related measurements in the range plots. It can also be noted that filter continues to estimate even when the probability of detection P_D drops to zero and no target-generated measurements are present.

Finally, the results using the r-JoTT filter are shown in Figures 15a and 15b. To evaluate how do the probability of existence q and the probability of detection are related, in the case of the r-JoTT filter, the probability of survival P_S was set o 99.99%. As can be observed from the figure, the estimated number of clutter measurements λ_Θ, in general, is below zero and one. The explanation for this is the result of the CFAR processing. CFAR processor produces empty detection sets for the observations where no appropriate signal strength peaks were detected. As explained in [14], the majority of CFAR-processed radar scans are empty, thus leading the λ_Θ estimate to be less than one.

6.2 Vision-Based Results

6.2.1 Pre-processing of the images

An important pre-processing step to perform object detection and/or tracking is the reduction of noise in the images. Bright objects such as stars may result in incorrect detections of Near Earth Object (NEO)s. As explained in Section 5, the software SExtractor [3] is used to detect stars, but also returns intermediate images obtained during the process including background estimate image, background-subtracted image, segmented object image and background-subtracted image with objects removed. These images can be seen in Figure 16, the negative of the images is used for more clarity.

Adjusting some parameters is necessary to remove most of the stars and to maintain all the NEOs. `DETECT_THRESH` is an important parameter, set to 3.5. It indicates the value at which the pixels are considered objects. In this case the threshold is 3.5 times the standard deviation of the estimated

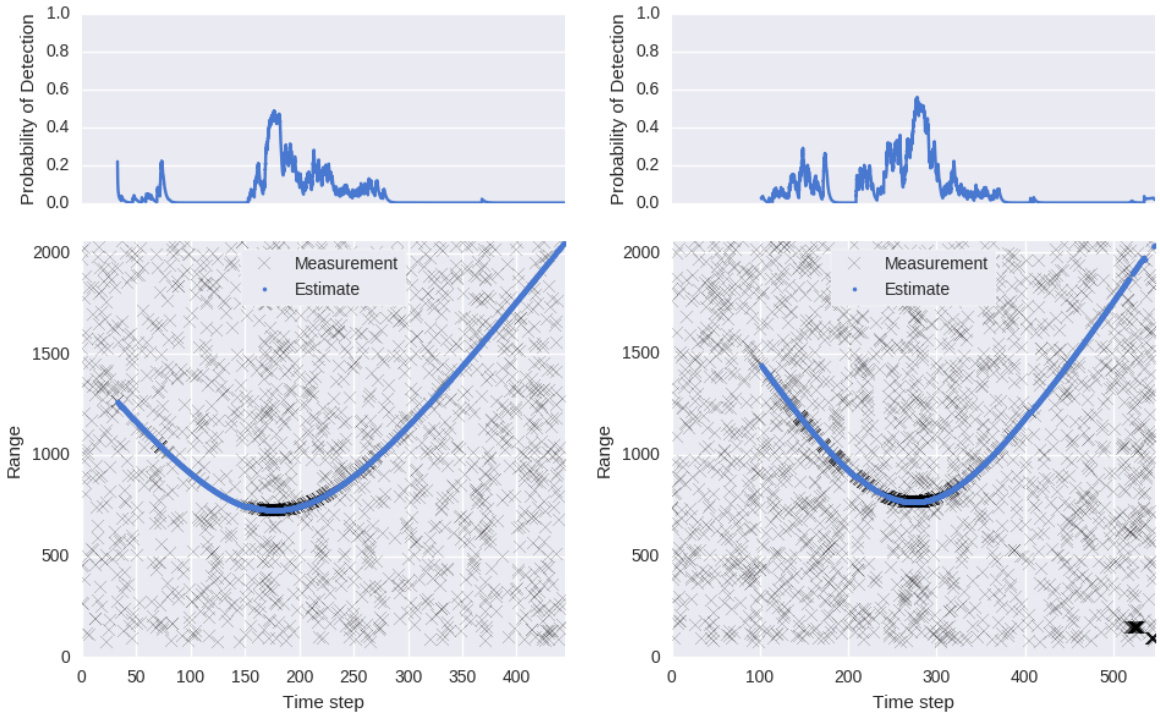

(a) βGM-JoTT filter estimates for the GPM satellite pass (I).

(b) βGM-JoTT filter estimates for the GPM satellite pass (II).

Figure 14: Results of real-world multiple-measurement CAMRa data sets using the βGM-JoTT filter.

background. `DETECT_MINAREA` was set to 3 which indicates the minimum area or number of adjacent pixels for object detection. The chosen filter was a 3×3 top-hat filter, included in the SExtractor folder, tophat_2.5_3x3.conv. The filter has the function of highlighting interesting pixels and reducing the noise level. `DEBLEND_NTHRESH` is set to 16 and `DEBLEND_MINCONT` to 0.00005. Both parameters are necessary to determine how the algorithm splits adjacent pixels belonging to different objects, recursively. For background noise estimation `BACK_SIZE` is set to 24, `BACK_FILTERSIZE` to 5, `BACKPHOTO_THICK` to 24, while other parameters are set to their default values. More details of the software can be found in [3] or [9].

6.2.2 TLE projection over the images

NEOs are seen as straight lines in the images. The length of the line depends on the distance from the object to the Earth and the exposure time of the photograph. The TLEs contain information of the cataloged debris orbiting the Earth, therefore an experiment was carried out to project the objects presented in this catalog to the image in order to match them with the straight lines of the images. The used TLE was obtained from "http://space-track.org". A TLE record from the date nearest to the date of the observations must be used to give the highest accuracy and if possible from the same day. The PyEphem library [15] from Python was used to read the TLE, and predict the object position at the same time the photograph was taken. PyEphem internally uses the SGP4 from SGP model, and provides accurate astronomical computations. Given a date and location on the Earth, it predicts the location of satellites, planets, and other objects in different coordinate systems. Highly correlated matches between the images and the TLE objects are shown in Figure 17. Blue stright lines correspond to the projected debris from the catalog and in red the name of the object in the catalog is provided. Note that the blue lines are drawn over or beside the debris straight line, which show how close the projected and the real debris are.

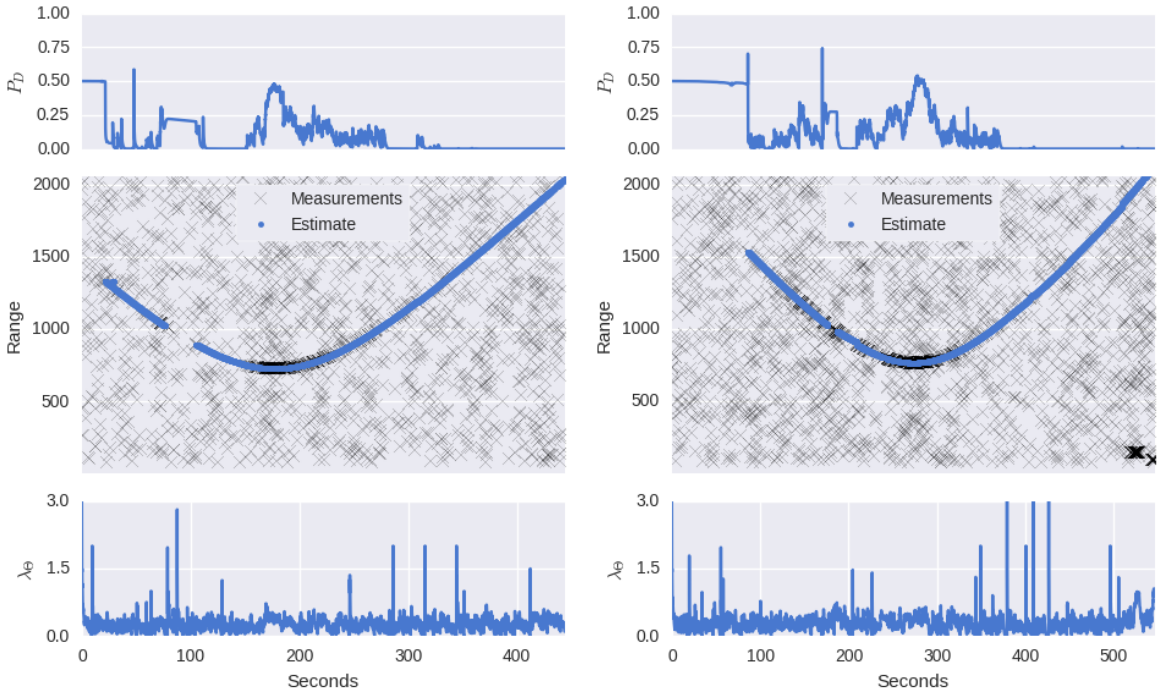

(a) r-JoTT filter estimates for the GPM satellite pass (I).

(b) r-JoTT filter estimates for the GPM satellite pass (II).

Figure 15: Results of real-world multiple-measurement CAMRa data sets using the r-JoTT filter.

7 Discussion and Future Work

During this period, extensions to the JoTT filter to account for unknown detection statistics were developed, and initial work on detecting orbiting objects from visual data was carried out.

Two extensions to the JoTT filter were developed. First, to account for an unknown and possible time varying probability of detection, the βGM-JoTT was developed. Second, to further account for unknown clutter rate, the r-JoTT filter was developed. These extensions were evaluated using simulated data and used in real data from the CAMRa radar.

Future directions related to the JoTT filter are:

- Investigate methods to account for unknown birth of a target.
- Implementation and evaluation of forward-backward smoothing [20] and the extension of the smoothing algorithm for the robust versions of the JoTT filter.
- Comprehensive approach to peak (detection) extraction from line of sight measurements of CAMRa.
- Use the complete radar measurement, i.e. using track before detect, into the JoTT filter framework.

In order to advance in vision-based RFS tracking, images for the Falcon project are waited. In the meanwhile a synthetic database will be build based on the OmniSSA database characteristics, and RFS algorithms will be applied on them.

7.1 Publications

The following is a list of publication related to the Grant No. FA9550-15-1-0069.

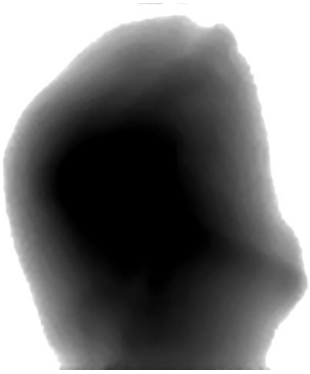

(a) Background estimation of the image ($I_B(x, y)$).

(b) Background-subtracted image ($I_F(x, y)$).

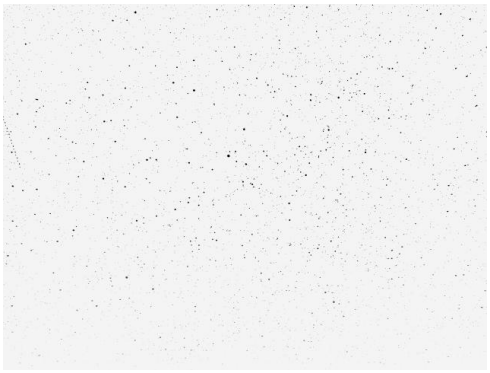

(c) Segmented objects from the image ($I_S(x, y)$).

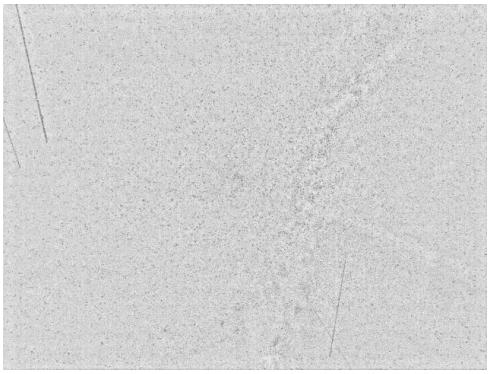

(d) Background-subtracted image in which stars are removed ($I_R(x, y)$).

Figure 16: Negative of images obtained during the process of object detection by SExtractor.

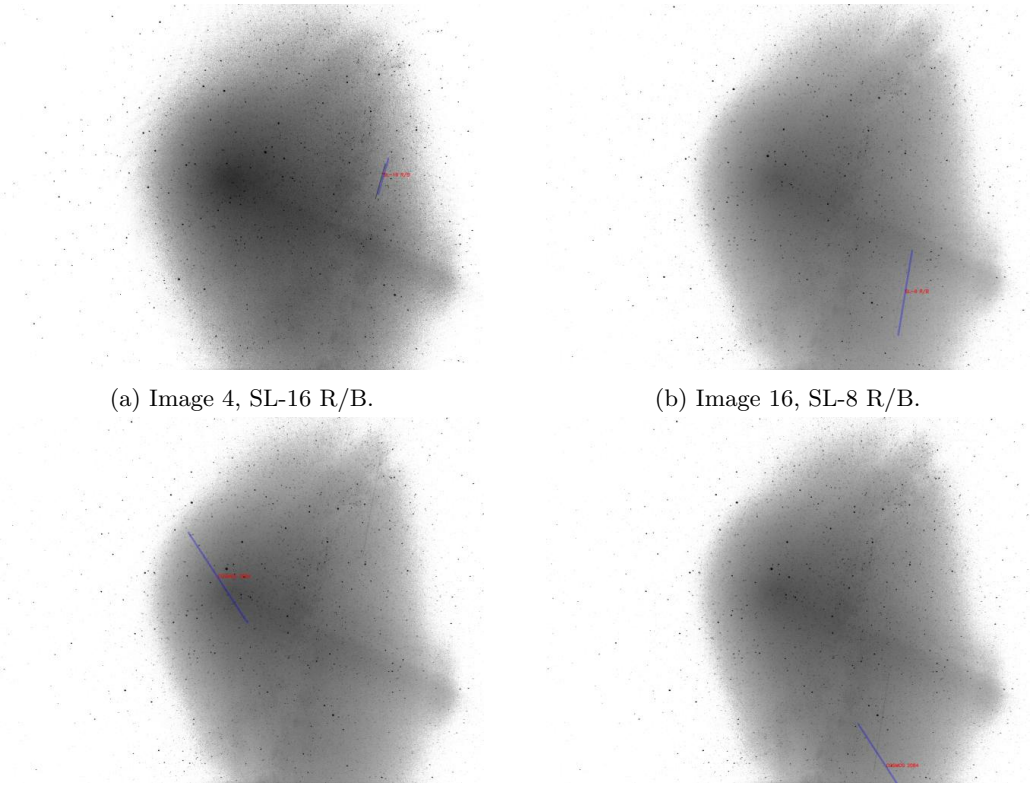

(a) Image 4, SL-16 R/B.

(b) Image 16, SL-8 R/B.

(c) Image 14, Cosmos 2084.

(d) Image 15, Cosmos 2084.

Figure 17: Debris match between the TLE catalog and the image straight lines. In blue the projected debris from the catalog, in red the name of the object in the catalog.

- Joint Target Detection and Tracking Filter for Chilbolton Advanced Meteorological Radar Data Processing. A. Pak, J. Correa, M. Adams, D. Clark, E. Delande, J. Houssineau, J. Franco, C. Frueh. In*Proceedings of 17 Advanced Maui Optical and Space Surveillance Conference (AMOS)*, Maui, Hawaii, September 2016

- Robust Joint Target Detection and Tracking for Space Situational Awareness. A. Pak, J. Correa, M. Adams. In submission to *Journal of Guidance, Control and Dynamics, Special Issue on Space Domain Awareness*. 2017

References

[1] Martin Adams, John Mullane, Ebi Jose, and Ba-Ngu Vo. *Robotic Navigation and Mapping with RADAR*. Artech House, London, 2012.

[2] E Bertin. Sextractor users manual, 2006.

[3] Emmanuel Bertin and Stephane Arnouts. Sextractor: Software for source extraction. *Astronomy and Astrophysics Supplement Series*, 117(2):393–404, 1996.

[4] William M. Bolstad. *Introduction to Bayesian Statistics*. Springer-Verlag New York, Inc., John Wiley and Sons, Inc., Hoboken, New Jersey. USA, 2007.

[5] JD Eastment, DN Ladd, CJ Walden, RP Donnelly, A Ash, NM Harwood, C Smith, JC Bennett, I Ritchie, M Rutten, et al. Technical description of radar and optical sensors contributing to joint uk-australian satellite tracking, data-fusion and cueing experiment. In *Advanced Maui Optical and Space Surveillance Technologies Conference*, volume 1, page 12, 2014.

[6] John G Fryer and Duane C Brown. Lens distortion for close-range photogrammetry. *Photogrammetric engineering and remote sensing*, 52(1):51–58, 1986.

[7] M Grøtte, S Virani, M Holzinger, A Register, C Perez, and J Tapia. All-sky image fusion for a synoptic survey telescope in arctic and antarctic domains. In *Advanced Maui Optical and Space Surveillance Technologies Conference*, 2016.

[8] Erik Høg, Claus Fabricius, Valeri V Makarov, S Urban, T Corbin, G Wycoff, Ulrich Bastian, Peter Schwekendiek, and A Wicenec. The tycho-2 catalogue of the 2.5 million brightest stars. *Astronomy and Astrophysics*, 355:L27–L30, 2000.

[9] Benne W Holwerda. Source extractor for dummies v5. *arXiv preprint astro-ph/0512139*, 2005.

[10] S. J. Julier and J. K. Uhlmann. Unscented filtering and nonlinear estimation. *Proceedings of the IEEE*, 92(3):401–422, 2004.

[11] Dustin Lang, David W Hogg, Keir Mierle, Michael Blanton, and Sam Roweis. Astrometry. net: Blind astrometric calibration of arbitrary astronomical images. *The astronomical journal*, 139(5):1782, 2010.

[12] Mahler, Ronald P. S. *Statistical Multisource-Multitarget Information Fusion*. Artech House, Inc., Norwood, MA, USA, 2007.

[13] Mahler, R.P.S. *Advances in Statistical Multisource-Multitarget Information Fusion*. Artech House, Inc., Norwood, MA, USA, 2014.

[14] A Pak, J Correa, M Adams, D Clark, E Delande, J Houssineau, J Franco, and C Frueh. Joint target detection and tracking filter for chilbolton advanced meteorological radar data processing. In *Advanced Maui Optical and Space Surveillance Technologies Conference*, 2016.

[15] Brandon Craig Rhodes. Pyephem: Astronomical ephemeris for python. *Astrophysics Source Code Library*, 2011.

[16] Branko Ristic, Ba-Tuong Vo, Ba-Ngu Vo, and Alfonso Farina. A tutorial on bernoulli filters: theory, implementation and applications. *Signal Processing, IEEE Transactions on*, 61(13):3406–3430, 2013.

[17] W Romanishin. An introduction to astronomical photometry using ccds. *University of Oklahoma*, 17, 2006.

[18] Gene Stansbery. Nasa's orbital debris program office. briefing to the nasa advisory council. `https://www.nasa.gov/sites/default/files/files/OrbitalDebrisProgramOffice.pdf`. Accessed: 2016-03-28.

[19] Vallado, D. A. *Fundamentals of Astrodynamics and Applications.* Microcosm Press, 4^{th} edition, 2013.

[20] Ba-Ngu Vo, Ba-Tuong Vo, and Ronald PS Mahler. Closed-form solutions to forward–backward smoothing. *IEEE Transactions on Signal Processing*, 60(1):2–17, 2012.

[21] Ba Tuong Vo, Chong Meng See, Ning Ma, and Wee Teck Ng. Multi-sensor joint detection and tracking with the bernoulli filter. *IEEE Transactions on Aerospace and Electronic Systems*, 48(2):1385–1402, 2012.

Acronyms

β**GM** β-Gaussian Mixture.

CA Cell Averaging.

CAMRa Chilbolton Advanced Meteorological Radar.

CFAR Constant False Alarm Rate.

CPHD Cardinalized Probability Hypothesis Density.

EKF Extended Kalman Filter.

FITS Flexible Image Transport System.

GM Gaussian mixture.

GPM Global Precipitation Measurement.

IOD Initial Orbit Determination.

JoTT Joint Target Detection and Tracking.

LEO Low-Earth Orbit.

MAE Mean Absolute Error.

NEO Near Earth Object.

OmniSSA Omnidirectional Space Situational Awareness.

PHD Probability Hypothesis Density.

r-JoTT Robust JoTT.

RFS Random Finite Set.

RSOs Resident Space Objects.

SGP Simplified General Pertrubations.

SSN Space Surveillance Network.

TLE Two-Line Element.

UKF Unscented Kalman Filter.

WCS World Coordinate Systems.

Symbols

$\mathbf{x}, \mathbf{z}$	State and measurement vector.
$\mathbf{F}, \mathbf{H}$	Transition and observation matrices.
$\mathbf{Q}, \mathbf{R}$	Transition noise and measurement noise matrices.
$\mathbf{m}, \mathbf{P}$	Mean and covariance of a Normal distribution.
X, Z	State and measurement set.
$Z_{1:k}$	Measurement history from time step 1 to time step k.
Θ	Clutter RFS.
q	Probability of existence of a Bernoulli RFS.
$s(\mathbf{x})$	Spatial distribution of a Bernoulli RFS.
P_B, P_S, P_D	Birth, survival and detection probabilities.
$f_B(\mathbf{x})$	Spatial distribution of the born target.
$f_{k\|k-1}(\mathbf{x}_k\|\mathbf{x}_{k-1})$	Predictive distribution of the target at time step k given previous state.
$f_z(\mathbf{z}\|\mathbf{x})$	Measurement distribution given state.
$\kappa_\Theta(\mathbf{z})$	Spatial distribution of the clutter.
λ_Θ	Expected number of clutter measurements.
$G(\lambda; \alpha, \beta)$	Gamma distribution with parameters α and β.
$B(P_D; a, b)$	Beta distribution with parameters a and b.
$\Gamma(x)$	Gamma function.
$I(x, y)$	Original fits image.
$\bar{I}_{block}$	Median of an image block.
σ_{block}	Standard deviation of an image block.
$I_B(x, y)$	Background image.
$I_F(x, y)$	Background-subtracted image.
$I_S(x, y)$	Segmented image.
t_h	Threshold for object segmentation on Background-subtracted image.
$F_G(x, y)$	Gaussian filter.
$F_{th}(x, y)$	Top-hat filter.
$F_b(x, y)$	Block filter.
$F_{Mh}(x, y)$	Mexican-hat filter.